PCCP

RSC Publishing

PAPER

View Article Online
View Journal

Unusual molecular material formed through irreversible transformation and revealed by 4D electron microscopy†

Cite this: DOI: 10.1039/c3cp51011e

Renske M. van der Veen,[a] Antoine Tissot,[b] Andreas Hauser[b] and Ahmed H. Zewail*[a]

Four-dimensional (4D) electron microscopy (EM) uniquely combines the high spatial resolution to pinpoint individual nano-objects, with the high temporal resolution necessary to address the dynamics of their laser-induced transformation. Here, using 4D-EM, we demonstrate the *in situ* irreversible transformation of individual nanoparticles of the molecular framework Fe(pyrazine)Pt(CN)$_4$. The newly formed material exhibits an unusually large negative thermal expansion (*i.e.* contraction), which is revealed by time-resolved imaging and diffraction. Negative thermal expansion is a unique property exhibited by only few materials. Here we show that the increased flexibility of the metal–cyanide framework after the removal of the bridging pyrazine ligands is responsible for the negative thermal expansion behavior of the new material. This *in situ* visualization of single nanostructures during reactions should be extendable to other classes of reactive systems.

Received 7th March 2013,
Accepted 9th April 2013

DOI: 10.1039/c3cp51011e

www.rsc.org/pccp

Introduction

Most materials expand upon heating, and this expansion is understood in terms of the inherent anharmonicity of bond vibrations. The opposite behavior, namely contraction, that is, the counter-intuitive *decrease* in volume or length of a material with increasing temperature, is a property exhibited by relatively few materials.[1,2] At the fundamental level, one must relate the contraction with a negative thermal expansion (NTE) to features beyond bond-stretching vibrations and isotropic heating of the material. From a technological point of view, the NTE phenomenon is significant, because it provides the possibility for compensating the ubiquitous positive thermal expansion (PTE) of common materials and merging them into NTE–PTE composites for optical and electronic device applications.

Metal-oxide frameworks with single-atom bridges, such as ZrW_2O_8 and Cu_2O, are among the most studied NTE materials.[3,4] More recently, the unusually large negative expansion properties of cyanide-bridged molecular framework materials were recognized.[5–8] The NTE behavior in these bridged compounds was attributed to the thermal population of low-energy transverse vibrational modes of the bridging moieties away from the metal–metal axes, resulting in negligible positive expansion of individual bond distances.[5] Compared to the rigid single-atom oxide bridges, the underconstrained cyanide (CN) ligands significantly increase the dynamic flexibility of the framework, providing a large number of low-frequency flexing (rather than stretching) modes that are responsible for the NTE observed in these systems.

Hitherto, the spatiotemporal behavior of NTE has not been reported. Such studies enable visualization of structural change and its temporal behavior. Here, we employ 4D electron microscopy,[9,10] with *in situ* photothermal excitation and time-resolved single-nanoparticle imaging and diffraction capabilities, to directly visualize NTE of molecular framework nanoparticles. The starting material is the spin-crossover compound Fe^{II}(pyrazine)$Pt^{II}(CN)_4$ in the form of plate-like nanocrystals (Fig. 1A–C), which exhibits a cooperative first-order phase transition from a diamagnetic low-spin state to a paramagnetic high-spin state around 250 K (Fig. 1D and E).[11–13]

Our previous 4D electron microscopy work on this compound has demonstrated the reversible thermoswitching, between low- and high-spin phases of single Fe(pyrazine)Pt(CN)$_4$ nanoparticles excited by short pulses of laser light.[14] The unit cell expansion was mapped in real- and reciprocal-space. Although a small

[a] *Physical Biology Center for Ultrafast Science and Technology, Arthur Amos Noyes Laboratory of Chemical Physics, California Institute of Technology, Pasadena, CA 91125, USA. E-mail: zewail@caltech.edu*

[b] *Département de Chimie Physique, Université de Genève, CH-1211 Genève, Switzerland*

† Electronic supplementary information (ESI) available: See DOI: 10.1039/c3cp51011e

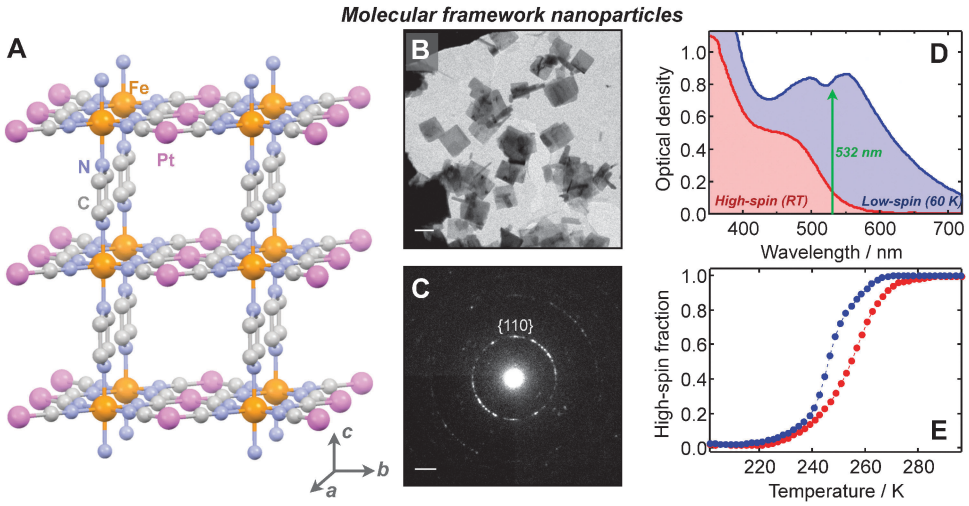

Fig. 1 (A) Crystal structure of Fe(pyrazine)$Pt(CN)_4$.[11] The axial pyrazine ligands are shown in one specific orientation for clarity; they are rotationally disordered in the actual structure. The hydrogen atoms are omitted for clarity. (B) Electron microscopy bright-field image and (C) diffraction pattern of an ensemble of Fe(pyrazine)$Pt(CN)_4$ nanoplatelets at 90 K. The {110} reflection ring is labeled in the pattern. The scale bar in the image is 500 nm, the one in the diffraction pattern is 1 nm^{-1}. (D) Optical absorption spectra of the low- and high-spin phases at 60 K and RT, respectively. The excitation wavelength is denoted as a green arrow. The absorption band in the visible is assigned to a metal-to-ligand charge-transfer (MLCT) transition from the Fe to the pyrazine ligand. (E) Phase transition heating and cooling curves obtained by recording the absorption at 570 nm. The high-spin fraction was obtained from normalizing the absorption values in D (assuming 100% low-spin at 60 K and 100% high-spin at RT).

negative thermal volume expansion was reported for the low-spin state of this compound ($\alpha_{vol} = dV/V\,dT = -2 \times 10^{-5}$ K^{-1}),[15] its involvement was minor compared to the much larger positive expansion induced by the spin transition.

In this study, we demonstrate that a fraction of Fe(pyrazine)-$Pt(CN)_4$ nanoparticles undergo an irreversible phase transformation upon photothermal excitation, *i.e.* the combined laser photon excitation and the resulting temperature jump. Surprisingly, the formed particles *contract* on the nanometer scale when thermally excited, providing evidence for the synthesis of a new material with an unusually large negative thermal expansion coefficient. Besides these spatiotemporal studies through time-resolved imaging and diffraction, we also employed powder X-ray diffraction and thermogravimetric analysis in order to address the nature of the structure formed in the irreversible transformation.

Materials and methods

Sample preparation and characterization

The synthesis of the Fe(pyrazine)$Pt(CN)_4$ nanoparticles was adapted from ref. 16. First, two aqueous solutions of reactants were prepared: (a) 0.2 mmol of $Fe(BF_4)_2{\cdot}H_2O$ + 0.8 mmol of pyrazine (in excess) dissolved in 4 mL of deionized water, and (b) 0.2 mmol of $K_2Pt(CN)_4$ dissolved in 4 mL of deionized water. Then, two starting micro-emulsions were prepared by the slow addition of these aqueous solutions to 44.5 mmol of dioctyl sodium sulfosuccinate (NaAOT) previously dissolved in 88 mL of *n*-heptane. Both solutions were stirred until stabilization and then quickly mixed under intensive stirring. Orange precipitates began to appear after one hour of stirring. After 24 h, the precipitate was collected by centrifugation (10 min. at 10 000 rpm) and washed several times by redispersion in ethanol and centrifugation to remove the traces of surfactant around the particles.

Powder X-ray diffraction (XRD) measurements were performed with a Bruker D8 Advance diffractometer equipped with a Cu Kα X-ray source in a Bragg–Brentano geometry. Patterns were registered between 5 and 40° with 3 h integration time. Thermogravimetric analysis (TGA) was performed with a Netzsch Jupiter STA 449 F3 machine at a scan speed of 20 °C min^{-1} between 25 and 800 °C.

For the 4D electron microscopy experiments, the nanoparticle powder was dispersed in ethanol and sonicated for 20 s. A small droplet (~7 μl) of the solution was delivered onto a graphite substrate on a 2000 mesh Cu frame and dried in air. The grid was heated at 110 °C for 2 h to remove residual crystal water. Between measurements on different days, the sample was kept under vacuum and heated at 90 °C for 3 h; it was transported in a liquid-nitrogen cryo-holder and kept at 90 K.

4D electron microscopy methodology

Overviews of the concept of 4D-EM and apparatus are detailed elsewhere.[10] Briefly, Caltech's second-generation apparatus is equipped to deliver fs and ns electron pulses; here we invoked the ~10 ns electron pulses (200 keV) generated through photoemission from a LaB_6 cathode which is incorporated in a FEG gun assembly. A short ~7 ns laser pulse at 532 nm (8 mJ cm^{-2}) excites the nanoparticle and the subsequent dynamics are probed by the similarly short electron pulse, mutually synchronized at a repetition rate of 3 kHz. The delay between pump and probe pulses was varied electronically, such that structural dynamics of the nanoparticle are mapped in real time.

The laser is guided onto the sample by a mirror inside the microscope column with an angle of $\sim 5^{\circ}$ with respect to the incoming electron beam; the laser polarisation is approximately parallel to the sample plane. The power and pointing stability of the laser beam was monitored *in situ* by a beam profiler camera located at an equivalent image plane of the specimen. Slight laser beam drifts between measurements were corrected for. The beam size and fluence were also obtained from the beam profiler image.

The spatial selection of the particles is performed by placing a small selected-area diffraction (SAD) aperture in the image plane of the objective lens in the TEM. The smallest aperture was used for the single particles, with a projected size in the sample plane of ~ 1 μm. The alignment of the SAD aperture was verified and corrected for by comparing the selected area in the image with the shadow image of the defocused direct beam in diffraction. The camera length and the ellipticity in the measurement of diffraction patterns were calibrated and corrected for, respectively, using a polycrystalline aluminum film as a reference.

Dynamics quantification

Because the specimen at low-temperature is prone to slight temperature fluctuations, the drift in the sample plane was appreciable (5–10 nm min^{-1}). By keeping the total acquisition time of the scans short, we made sure that the nanoparticles stay within the view of the selecting aperture. For typical acquisition times per image or diffraction pattern of 10 s, 100 delay steps per scan result in an acceptable drift of $\sim$100–200 nm. In order to quantify the dynamics and to produce the 4D nano-movies, we employed post-acquisition drift correction based on image cross-correlation. A small recognizable area in the image was selected, and for each time delay the cross-correlation matrix with respect to a reference image before $t = 0$ was calculated using FFT procedures. The necessary drift correction to obtain maximum cross-correlation was derived. This procedure was also applied to the diffraction patterns, which undergo drifts due to magnetic hysteresis of the imaging lenses of the microscope.

The diffraction dynamics were quantified by 2D Gaussian fitting of the diffraction peaks, which were paired according to the inversion symmetry of the diffraction pattern (Friedel pairs). Prior to peak fitting a median filter was applied to the diffraction patterns. Each diffraction pattern in a time-delay scan was normalized to the total integrated intensity. No laser-induced intensity/width changes of the direct beam were observed, which excludes possible laser-induced charging effects on the sample. Several time profiles (typically 5, including forward and reverse delay scans) were averaged together during data processing.

Real-space dynamics were quantified by taking line profiles along the two perpendicular directions of the square nanoparticles. For each line profile, the image intensity was integrated along the mutually perpendicular direction up to the particle borders. By taking the derivative of the resulting cross-sections, the edge positions could be accurately determined. All images were normalized to the totally integrated intensity in an area of the image showing only the substrate.

Results

In situ irreversible transformation

Fig. 2 depicts the single-nanoparticle bright-field images and electron diffraction patterns before (A and B) and after (C and D) exposing the particle to a train of ~ 7 ns laser pulses (532 nm, 3 kHz, 8 mJ cm^{-2}) at 90 K equilibrium temperature. On a time scale of tens of seconds, the particle shrinks, looses its distinct diffraction contrast and its electron diffraction pattern becomes quite broad. What at first seems to be a damage of the nanoparticle, eventually appears to be an irreversible phase transformation originating from the well-known crystal structure of Fe(pyrazine)$Pt(CN)_4$.[11,15] The appearance of the nanoparticle and its diffraction pattern remains unchanged after the phase transformation, even under further light irradiation.

The diffraction pattern of the original Fe(pyrazine)$Pt(CN)_4$ nanoparticle (Fig. 2B) exhibits sharp reflections that can be indexed for an incoming beam direction nearly coincident with the [001] zone axis, in good agreement with the published tetragonal low-spin structure.[11,15] The sharpness of the diffraction pattern and the strong diffraction contrast in the image demonstrate the excellent 3D crystallinity of the nanoparticle. The hexagonal diffraction pattern of the underlying graphite substrate ($\sim$5–10 graphene layers) is also visible.

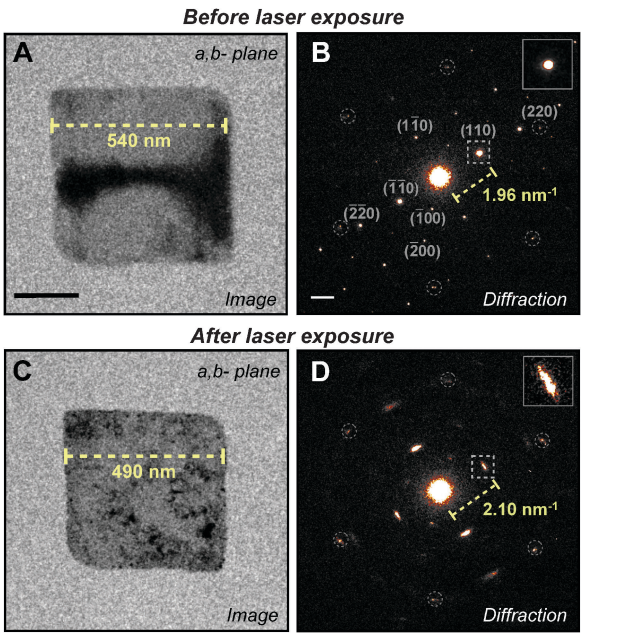

Fig. 2 Single-nanoparticle bright-field images and diffraction patterns before (A, B) and after (C, D) *in situ* photothermal phase transformation (90 K, 4° tilt). The scale bar in the image is 200 nm, the one in the diffraction pattern is 1 nm^{-1}. The incoming electron beam is (almost) perpendicular to the particle surface coinciding with the *a,b*-crystal plane. The diffraction pattern (B) can be indexed in the tetragonal space group of the low-spin Fe(pyrazine)$Pt(CN)_4$ structure (see labels). A zoom into one of the {110} peaks (dashed boxes) is shown in the upper right corner of the diffraction patterns. Note the more diffuse appearance of the pattern after the transformation. The value of the {110}-momentum transfer and the particle dimensions are denoted in the patterns/images for comparison. The dashed circles depict the hexagonal diffraction pattern from the underlying graphite substrate.

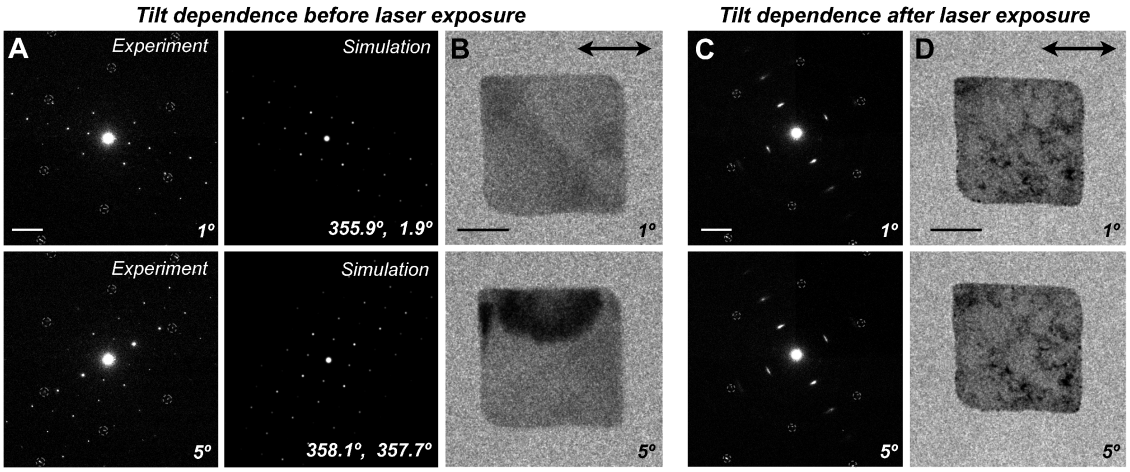

Fig. 3 Tilt dependence of single-nanoparticle diffraction patterns *before* (A, B) and after (C, D) the irreversible phase transformation. The sample is rotated around an axis lying in the plane of the substrate, indicated by the black arrow. A median filter was applied to the diffraction patterns in order to enhance the contrast. Kinematical electron diffraction simulations[20] for a particle thickness of 5 nm are shown to the right of each diffraction pattern in (A) (the two angles denote rotation around the *a*- and *b*-axes, respectively). The scale bar in the diffraction patterns is 2 nm^{-1} and the dashed circles depict the hexagonal diffraction pattern from the underlying graphite substrate (not simulated). The scale bar in the images is 200 nm.

In contrast, the diffraction pattern of the new phase after the transformation (Fig. 2D) exhibits broad peaks extended into small ring segments along the azimuthal angle. It is noted that the strongest reflections in the original diffraction pattern – {110}, {220}, {100}, {200}‡ – have their counterparts in the pattern after the transformation, although they are broadened and shifted to larger momentum transfer values. This implicates shorter lattice spacings in the *a,b*-plane of the new crystal phase, which is corroborated by the appreciably smaller nanoparticle dimensions (Fig. 2A and C), while the tetragonal crystal symmetry is preserved.

By simulating the diffraction patterns of Fe(pyrazine)$Pt(CN)_4$ for different sample tilt angles (Fig. 3A), the nanoparticle thickness was estimated to be ~5–10 nm; for a thicker nanoparticle the higher-order reflections at large scattering angles cannot be simulated symmetrically at opposite sides of the direct beam (as in the experimental patterns). In reciprocal-space terms: the thicker the particle, the sharper the reciprocal lattice points, and the more sensitive the diffraction pattern becomes for small tilt changes. For very thin particles, the reciprocal lattice points are broadened into rods along the *c*-direction, and the Ewald sphere intercepts these rods at high scattering angles with the direct beam (almost) along the [001] zone axis. For thicker particles, these reflections would not be visible.

At certain tilt angles, the diffraction contrast changes abruptly, as shown in Fig. 3B for a tilt angle of 5°. In contrast, the diffraction pattern and image of the nanoparticle after the transformation remain nearly unaffected as the sample tilt angle is changed, as demonstrated in Fig. 3C and D. More images and diffraction patterns at various tilt angles are given in the ESI† (Fig. S1–S4).

‡ {*hkl*} denotes the whole family of planes, *i.e.* the set of all planes that are equivalent to (*hkl*) by the symmetry of the lattice (here tetragonal).

Real- and reciprocal-space imaging of the new phase

The unusual properties of the new phase are evidenced by the large contraction observed in a stroboscopic time-resolved laser pump–electron probe experiment (532 nm, 3 kHz, 8 mJ cm^{-2}). The photons are absorbed mainly by the graphite substrate, whereby electron–phonon coupling quickly converts the photon energy into heat, causing a temperature jump as high as ~700 K for a laser fluence of 8 mJ cm^{-2}. Because of the extremely high thermal conductivity of graphite, the heat is dissipated within only ~150 ns to the surrounding copper frame (see ESI,† Fig. S5).§

In Fig. 4A, we display the static bright-field image and representative time-framed difference images of the real-space expansion dynamics of a single nanoparticle (at 90 K) that has undergone the irreversible phase transformation previously described (different particle than before). The difference images were obtained by subtracting the (averaged) image of several frames before $t = 0$ from each frame taken at different $t > 0$ delay times. The white contours indicate that the nanoparticle isotropically shrinks upon excitation, which is more quantitatively depicted in Fig. 4B when plotting the relative change in particle dimensions along the two principal axes as a function of time delay. The particle contraction is as much as 11 nm at $t = +70$ ns, 1.8% of its equilibrium dimension (595 nm), and very short-lived (~150 ns). Real-space imaging and difference-imaging nano-movies of the negative expansion dynamics are provided as ESI† (nano-movies S1 and S2).

The real-space imaging is corroborated by stroboscopic single-nanoparticle diffraction measurements. The inset in Fig. 5A shows the difference diffraction pattern for $t = +70$ ns, referenced to the pattern at $t = -100$ ns. The shift of the diffraction peaks towards larger momentum transfer values

§ The time scale for heat dissipation depends on the exact geometry of the substrate and in particular the dimensions of the film with respect to the supporting copper frame that acts as a heat sink. In the present case the graphite film dimensions are 7.5 × 7.5 μm^2.

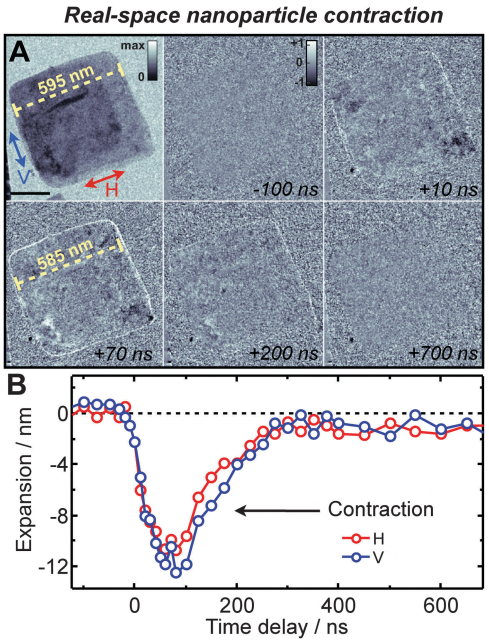

Fig. 4 (A) Bright-field and representative image difference maps at various time delays with respect to the laser excitation pulse. In the difference images, the white contours depict regions with increased intensity after excitation, implying a contraction (*i.e.* negative expansion) of the nanoparticle. The red and blue arrows denote the directions used to quantify the contraction dynamics as shown in panel B. The yellow lines indicate the particle dimensions before (595 nm) and +70 ns after excitation (585 nm). (B) Quantification of the particle dimension dynamics. The relative change in the particle size along the two principal directions denoted in A is plotted as a function of time delay.

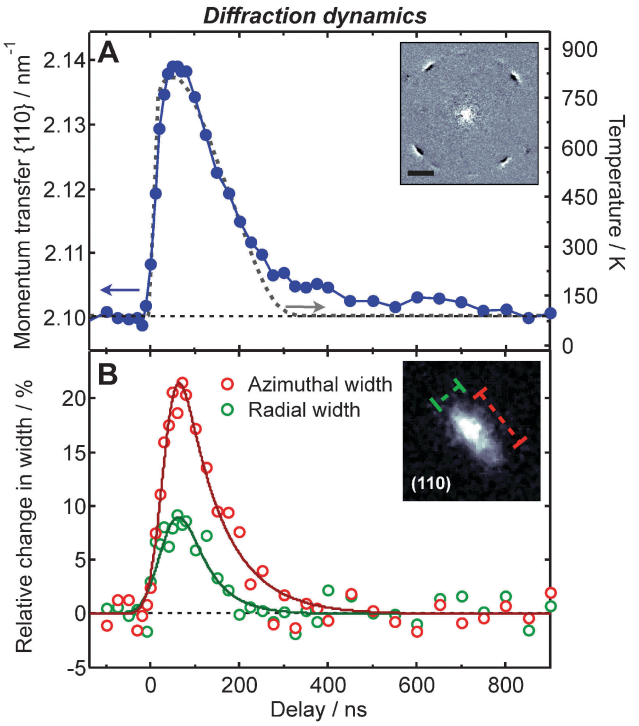

Fig. 5 (A) {110} Diffraction peak position as a function of time delay after photothermal excitation at 532 nm and a fluence of 8 mJ cm^{-2}. The dashed curve (right axis) denotes the simulated temperature profile in the nanoparticle (equilibrium temperature 90 K). The inset shows the diffraction difference map at t = +70 ns referenced to the pattern before excitation (scale bar 1 nm^{-1}). The increase in momentum transfer evidences a decrease in lattice spacing. (B) Relative azimuthal and radial {110} peak width dynamics referenced to the peak width before excitation. The inset shows a zoom into the {110} peak denoting the two peak width directions.

indicates the decrease in lattice spacings in the *a,b*-plane. The changes were quantified by 2D Gaussian peak fitting, with position, amplitude and two different peak width parameters for the radial and azimuthal directions of the diffraction pattern.

The response of the {110} diffraction peak position is depicted in Fig. 5A. The relative increase in the momentum transfer value of 1.9%, and the exponential decay time of ~140 ns, are in good agreement with the real-space image dynamics. Quantitatively, it corresponds to a decrease in the *a,b*-unit cell parameters from 6.73 Å before excitation to 6.61 Å at t = +70 ns. Concomitant with the shift, the peaks broaden significantly in both radial and, in particular, for the azimuthal directions (Fig. 5B). A simple model for heat generation and diffusion in the coupled graphite–nanoparticle system (see ESI† for details) was employed to derive the temperature jump induced in the nanoparticle (see dashed line and right axis in Fig. 5A). At +70 ns, a maximum temperature of ~800 K is reached. In addition, the time scale of the expansion dynamics is well reproduced by the simulated temperature profile of the nanoparticle.¶

Discussion

The molecular mechanism

Based on the above observations, we believe that the removal of pyrazine ligands from the framework structure is responsible for the irreversible phase transformation, as schematically depicted in Fig. 6A. Indeed, thermogravimetric analysis (TGA) on a powder of Fe(pyrazine)Pt(CN)$_4$·2H$_2$O nanoparticles (Fig. 7A) shows that in the temperature range from room temperature to 700 K two steps can be discerned: the first step (mass change: measured −8.25%; theoretical −7.5%) corresponds to the loss of water molecules, the second step between 500–700 K involves elimination of almost all pyrazine molecules (mass change: measured −15.6%; theoretical −16.7%), in good agreement with previously measured TGA on this compound.[11] Temperatures up to ~800 K are reached in the stroboscopic pulsed experiments, *i.e.* well in the range of thermal elimination of the pyrazine molecules.

We note that not all nanoparticles convert into the new phase. From the approximately fifteen different particles that were studied, three showed the above irreversible behavior; the others followed the spin-crossover dynamics reported in ref. 14. It is found that in the fraction that undergoes the irreversible reaction, the particles are thinner than those that undergo the

¶ The small discrepancies between the experimental and simulated profiles can be due to the simplicity of the model employed; in particular, approximations made for the optical and temperature-dependent thermal properties of the graphite substrate, the nanoparticle heat capacity, and possible non-linearity of the nanoparticle's expansion coefficient.

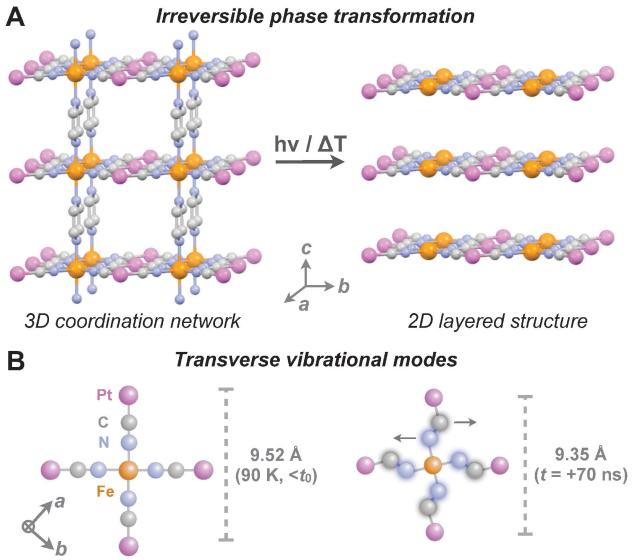

Fig. 6 (A) Schematic of the proposed irreversible phase transformation upon laser irradiation. The 3-dimensional (3D) framework structure is converted into a 2-dimensional (2D), graphite-like, layered structure without pyrazine ligands; (B) structural schematics demonstrating the transverse vibrational modes responsible for the negative thermal expansion in the *a,b* $FePt(CN)_4$ plane. Depicted is only one snapshot during a specific vibrational mode for one coordination sphere; in reality, the contraction involves many different low-energy modes which are highly dynamic and coupled between coordination spheres in the planes. Also at 90 K before excitation ($<t_0$) such modes are excited (not shown). The axial ligands are not shown for clarity.

spin-crossover ($\sim$5–10 nm, compared to >30 nm for the latter). The thin particles reach higher temperatures, allowing them to undergo the thermal elimination process, whereas the thicker particles remain in the temperature range of the spin crossover phase transition (200–400 K). Moreover, the large surface-to-volume ratio of the thin particles facilitates the escape of pyrazine molecules from their structure.

While the 2D $FePt(CN)_4$ sheets were tightly connected by the pyrazine ligands in the initial phase, they would be detached in the new phase. A loosely bound 2D layered structure, similar to graphite, is in good agreement with the observed diffraction pattern after phase transformation (Fig. 2D). In particular, the azimuthally broadened diffraction peaks indicate a rotational disorder of the *a,b*-planes around the [001] axis. Whereas such rotations are inhibited in the 3D crystalline pyrazine-bridged structure (evidenced by the very sharp {110} diffraction peaks), they become possible in the 2D layered structure without covalent bonds between the sheets. The insensitivity of the diffraction pattern to sample tilts indicates a deteriorated crystallinity along the *c*-axis direction (and possibly a decreased intersheet separation), which also agrees with the suggested layered structure lacking spacer molecules. Finally, the reduced lattice constants in the new phase (a,b = 6.73 Å, compared to 7.21 Å in $Fe(pyrazine)Pt(CN)_4$), is likely due to the absence of steric hindrance between the axial rotationally disordered pyrazine ligands, and, as discussed below, the contraction of the lattice through the excitation of transverse vibrational modes in the $FePt(CN)_4$ planes (the latter can also be responsible for the broadening of the diffraction peaks).

In order to test whether the new phase can be synthesized on a large scale by static heating, we performed X-ray powder diffraction on an ensemble of $Fe(pyrazine)Pt(CN)_4 \cdot 2H_2O$ particles and compared the patterns before and after heating at 623 K (Fig. 7B). The overall disappearance of sharp diffraction peaks after thermal treatment is due to the loss of crystallinity. However, two small peaks at 17.1° and 34.6° remain, and can be identified as the {110} and {220} reflections which are shifted to higher scattering angles (*i.e.* corresponding to a contraction of the unit cell). This is in qualitative agreement with the changes in the single-nanoparticle electron diffraction patterns (Fig. 2). However, quantitatively the peak shifts, and thus the contraction, achieved by static heating are about four times smaller than those observed in the pulsed single-nanoparticle experiment (see ESI,† Fig. S6). In addition, the integrated peak intensity of the {110} reflection in the single-nanoparticle pattern after the phase transformation is about the same as

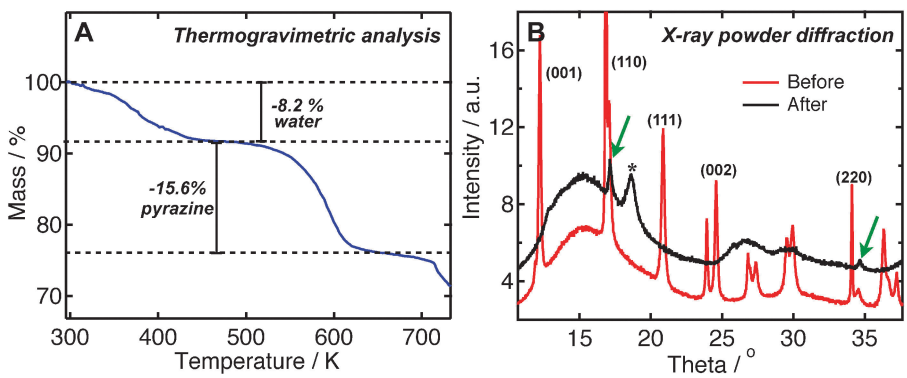

Fig. 7 (A) Thermogravimetric analysis of $Fe(pyrazine)Pt(CN)_4 \cdot 2H_2O$ nanoparticles. The two steps between room temperature and 700 K correspond to the loss of water molecule and pyrazine molecules, respectively. The quantitative mass losses represent nearly 100% of elimination. (B) Powder X-ray diffraction before (red) and after (black) thermal treatment of the $Fe(pyrazine)Pt(CN)_4 \cdot 2H_2O$ nanoparticles at 623 K. The most intense reflections before treatment are labeled. For clarity, the patterns are offset vertically and they are not corrected for the background from the sample holder. The two green arrows indicate two weak remaining peaks that can be identified as the shifted {110} and {220} reflections in the new phase, in analogy with the {110} and {220} reflections in the single-nanoparticle electron diffraction pattern (Fig. 2D). The new peak marked with a star is unidentified, but it likely arises from the decomposition products formed during the thermal treatment.

that of the original structure, whereas in the static-heating experiment the peak intensities are considerably reduced.

The above findings suggest that the new phase could indeed be formed by static heating, but along with many competing processes that reduce crystallinity. This is corroborated by infrared (IR) experiments on the nanoparticles before and after thermal treatment at 623 K (see ESI,† Fig. S7); the distinct absorption peak of the cyanide ligands in the Fe(pyrazine)$Pt(CN)_4$ structure, splits into two peaks after static heating, which indicates a reduced symmetry in the $FePt(CN)_4$ plane. This is not observed in the nanoparticle electron diffraction patterns.

We would like to note that in the 4D EM experiment only 20% of the particles underwent the transformation due to the fact that the temperature jump in these (thinner) particles was higher than in the other particles. In the static TGA experiment all particles reach an equally high temperature, yet only a small fraction seems to have undergone the transformation. The ultrafast (pulsed) heating mechanism thus more efficiently eliminates the pyrazine molecules from the framework while largely preserving the crystallinity of the *a,b*-planes.

At this point we should also mention the possibility of a photoinduced mechanism for pyrazine removal. The 532 nm laser pulse can excite the metal-to-ligand charge-transfer (MLCT) transition of the low-spin state (see Fig. 1D), promoting an electron from Fe(II) to the π^* orbitals of the pyrazine ligand. Such an excitation weakens the pyrazine bonds, resulting in a lower energy barrier for pyrazine decomposition, *e.g.* through intramolecular ring opening.[17] In addition, the selective deposit of heat in the form of excited vibrational modes of the pyrazine ligands, after relaxation of the MLCT state, could facilitate the thermal elimination of the pyrazine ligands. Due to the probing orientation in the current experiment (*i.e.* along the *c*-axis) we are at present not able to identify the exact nature of the potential axial ligands of the Fe(II) atoms.

Negative thermal expansion dynamics

In order to explain the thermal properties of the new phase, we note that the family of Prussian Blue analogues, $M^{II}Pt(CN)_6$ (M = Mn, Fe, Ni, Cd, Cu), was shown to exhibit negative thermal expansion behavior with expansion coefficients in the range -1×10^{-6} K^{-1} to -10×10^{-6} K^{-1}, depending on the metal atom.[18,19] ‖ The differences in thermal expansion magnitude are principally due to the different strengths of the metal–cyanide binding interaction. From the transient expansion dynamics and simulations (Fig. 5A) we derive a linear thermal expansion coefficient of $\sim -25 \times 10^{-6}$ K^{-1} in the *a,b* plane of the new crystal phase, which is in good agreement with the expansion coefficient of $\alpha_{a,b} = -30 \pm 5 \times 10^{-6}$ K^{-1} determined by measuring the {110} peak position as a function of temperature (without laser excitation, see ESI,† Fig. S8).

Compared to $FePt(CN)_6$ ($\alpha = -4 \times 10^{-6}$ K^{-1}), this negative expansion coefficient is unusually large, and at least 3 times larger than the largest coefficient reported in the $M^{II}Pt(CN)_6$ series.[19] The original compound Fe(pyrazine)$Pt(CN)_4$ was reported to have a negative volume expansion of -2×10^{-5} K^{-1};[15] but the linear expansion coefficients in the *a,b* and *c*-directions were not reported. The observation of a $\sim$1.5% *positive* linear expansion in the *a,b*-plane upon spin crossover with a temperature jump of 300 K,[14] puts a lower limit of 0.5% contraction due to negative thermal expansion, *i.e.* $\alpha_{a,b} > -15 \times 10^{-6}$ K^{-1} (100% spin crossover corresponds to 2% change in lattice parameter). We attribute the large expansion coefficient of the new material to the increased flexibility of the 2D $FePt(CN)_4$ sheets, as compared to the 3D ligand-bridged case.

In fact, in polymeric framework materials the local transverse distortion of cyanide bridges cannot be considered in isolation. The transverse vibrations are coupled into long-range, low-energy, acoustic rigid unit modes (RUMs) involving rotation and translation of undistorted metal coordination spheres (the distortion of which would require considerable energy),[6] as shown in projection for one such unit in Fig. 6B. As was demonstrated in the tetragonally distorted $CuPt(CN)_6$ framework,[19] the enhanced flexibility of the transverse cyanide modes along the Jahn–Teller elongated *c*-axis decreased the energy of correlated vibrations within the *a,b*-plane, leading to enhanced NTE behavior in the latter case ($\alpha = -5 \times 10^{-6}$ K^{-1}).

In analogy, here the exceptionally large negative expansion in the *a,b*-plane is due to the *decoupling* of the 2D $FePt(CN)_4$ sheets, rendering the low-energy lattice phonons in different sheets independent of each other. The significant increase in diffraction peak widths during the laser-induced contraction (Fig. 5B) indicates an increased rotational disorder and strain in the 2D planes upon thermal excitation. Indeed, the population of low-frequency acoustic RUMs responsible for the negative expansion introduces such long-range strain variations and dynamical inhomogeneity in lattice spacings.**

Conclusion

Here, we demonstrated the first *in situ* 4D visualization of single molecular framework nanoparticles undergoing an irreversible transformation. The observed exceptionally large contraction, *i.e.* negative thermal expansion, is unique and can be understood from knowledge of the change with time of both the diffraction and images of the material. The phase change upon photothermal excitation of the original Fe(pyrazine)$Pt(CN)_4$ structure provides material properties that cannot be explained by the conventional expansion mechanism (anharmonicity of bond vibrations). With such properties, the material may be used to build expansion-compensating composite structures. Future applications of 4D

‖ Formation of $FePt(CN)_6$ in the photothermal transformation can be excluded based on the symmetry of the observed diffraction pattern (*i.e.* tetragonal, whereas $FePt(CN)_6$ has cubic crystal symmetry), and on the fact that it would require whole $FePt(CN)_4$ sheets to shift with respect to each other in order to form the 3D Pt–CN–Fe network.

** In the present experiments the electron pulse propagates along the *c*-axis perpendicular to the *a,b*-plane and therefore we can not establish whether *c*-axis expansion is positive or negative in nature. However, based on the suggested 2D layered structure, and in analogy with graphite, we expect it to be a positive expansion.

electron microscopy should explore the reported single-nanoparticle imaging in order to study phenomena such as phase transition switching, thermal and mechanical nanoscale properties, and processes relevant to photocatalytic activity.

Acknowledgements

This work was supported by the National Science Foundation and the Air Force Office of Scientific Research in the Gordon and Betty Moore Center for Physical Biology at the California Institute of Technology. We thank Dr Oh-Hoon Kwon for assistance during the experiment and Dr Sang Tae Park for the helpful collaboration in the heat-transfer simulations. RMV acknowledges funding from the Swiss National Science Foundation.

References

1 C. Lind, *Materials*, 2012, **5**, 1125–1154.
2 W. Miller, C. W. Smith, D. S. Mackenzie and K. E. Evans, *J. Mater. Sci.*, 2009, **44**, 5441–5451.
3 T. A. Mary, J. S. Evans, T. Vogt and A. W. Sleight, *Science*, 1996, **272**, 90–92.
4 A. Sanson, F. Rocca, G. Dalba, P. Fornasini, R. Grisenti, M. Dapiaggi and G. Artioli, *Phys. Rev. B: Condens. Matter Mater. Phys.*, 2006, **73**, 214305.
5 P. J. Chupas and C. J. Kepert, *J. Am. Chem. Soc.*, 2005, **127**, 15630–15636.
6 A. Goodwin and C. Kepert, *Phys. Rev. B: Condens. Matter Mater. Phys.*, 2005, **71**, 140301.
7 A. L. Goodwin, M. Calleja, M. J. Conterio, M. T. Dove, J. S. O. Evans, D. A. Keen, L. Peters and M. G. Tucker, *Science*, 2008, **319**, 794–797.
8 A. E. Phillips, A. L. Goodwin, G. J. Halder, P. D. Southon and C. J. Kepert, *Angew. Chem., Int. Ed.*, 2008, **120**, 1418–1421.
9 A. H. Zewail, *Science*, 2010, **328**, 187–193.
10 A. H. Zewail and J. M. Thomas, *4D electron microscopy: imaging in space and time*, World Scientific Publishing, 2010.
11 V. Niel, J. Martinez-Agudo, M. Munoz, A. Gaspar and J. Real, *Inorg. Chem.*, 2001, **40**, 3838–3839.
12 S. Bonhommeau, G. Molnar, A. Galet, A. Zwick, J. Real, J. McGarvey and A. Bousseksou, *Angew. Chem., Int. Ed.*, 2005, **44**, 4069–4073.
13 F. Volatron, L. Catala, E. Riviere, A. Gloter, O. Stephan and T. Mallah, *Inorg. Chem.*, 2008, **47**, 6584–6586.
14 R. M. van der Veen, O.-H. Kwon, A. Tissot, A. Hauser and A. H. Zewail, *Nat. Chem*, 2013, DOI: 10.1038/NCHEM.1622.
15 S. Cobo, D. Ostrovskii, S. Bonhommeau, L. Vendier, G. Molnar, L. Salmon, K. Tanaka and A. Bousseksou, *J. Am. Chem. Soc.*, 2008, **130**, 9019–9024.
16 I. Boldog, A. B. Gaspar, V. Martinez, P. Pardo-Ibanez, V. Ksenofontov, A. Bhattacharjee, P. Guetlich and J. A. Real, *Angew. Chem., Int. Ed.*, 2008, **47**, 6433–6437.
17 W. D. Crow and C. Wentrup, *Tetrahedron Lett.*, 1968, 3115–3118.
18 A. L. Goodwin, K. W. Chapman and C. J. Kepert, *J. Am. Chem. Soc.*, 2005, **127**, 17980–17981.
19 K. W. Chapman, P. J. Chupas and C. J. Kepert, *J. Am. Chem. Soc.*, 2006, **128**, 7009–7014.
20 *CrystalMaker Software Ltd, Version 2.2.4*, Oxfordshire, UK.